batteries

MDPI

Article

Non-Destructive Mechanical Characterization of 4680 Cylindrical Lithium-Ion Cells for Cell-to-X Integration

Nima Ghandily [1,*], Rizwan Javed [2], Niklas Kisseler [1], Heiner Heimes [1] and Achim Kampker [1]

[1] Department Battery Engineering & Safety, Production Engineering of E-Mobility Components (PEM), RWTH Aachen University, 52056 Aachen, Germany; niklas.kisseler@rwth-aachen.de (N.K.); h.heimes@pem.rwth-aachen.de (H.H.); a.kampker@pem.rwth-aachen.de (A.K.)
[2] RheinNetz GmbH, 50823 Cologne, Germany; rizwan.javed@rwth-aachen.de
* Correspondence: nima.ghandily@rwth-aachen.de; Tel.: +49-151-5014-5741

Abstract

Electric vehicles offer a sustainable alternative to combustion engines but still face range and safety limitations. Integrating battery cells as structural elements (Cell-to-X, CTX) is a promising route to address both, but requires cells that reliably withstand everyday mechanical loads. This study presents a non-destructive mechanical characterization of commercial 4680-format cylindrical lithium-ion cells (Supplier 1), combining quasi-static compression tests (hemispherical and cylindrical indenters) across state of charge (SOC) and indentation depth, cyclic aging over up to 150 cycles, and post-mortem computed tomography (CT) analysis. Deformation remained predominantly reversible up to indentation depths of 0.5 mm for the hemispherical and 1.8 mm for the cylindrical indenter, and peak forces of up to 9.16 kN were sustained without functional or electrical failure, although localized plastic casing deformation was observed in individual cells at the highest tested depths. For the cylindrical indenter, peak force increased consistently with SOC and indentation depth, consistent with prior literature, while temperature and voltage remained stable throughout loading, with no immediate evidence of an internal short circuit. For the cells with a sufficiently complete cycling record, capacity loss over the valid cycles amounted to 1.8–2.9% per 100 cycles for the mechanically loaded cells, compared with 2.0% for an unstressed reference cell. Post-mortem CT imaging confirmed deformation remained confined to the outer casing and outermost jelly-roll layers without affecting internal structure or performance. These results provide preliminary evidence that the tested cells can tolerate structurally relevant mechanical loads without loss of function, supporting further development of CTX architectures.

Keywords: structural battery; 4680 cell; battery safety; cell-to-X; cell-to-pack; cell-to-chassis; deformation behavior

Academic Editors: Jie Liu and Xiaogang Wu

Received: 5 August 2026
Revised: 13 September 2026
Accepted: 16 September 2026
Published: 15 October 2026

Copyright: © 2026 by the authors. Licensee MDPI, Basel, Switzerland. This article is an open access article distributed under the terms and conditions of the Creative Commons Attribution (CC BY) license.

1. Introduction

In recent years, the automotive industry has witnessed a significant shift towards electrification, driven by the need for sustainable and environmentally friendly transportation solutions [1]. Electric vehicles (EVs) play a crucial role, with nearly 14 million new EVs in 2023, increasing the total number of EVs to 40 million worldwide. The increase in EV sales is driving higher demand for batteries, maintaining the upward trend of recent

years. Local energy demand in Europe for establishing domestic battery cell production and achieving self-sufficiency is projected to reach 250 TWh per year by 2050 [2].

The adoption of EVs has been accelerated by advancements in lithium-ion battery technology, which have played a pivotal role in enhancing the performance, range, and affordability of EVs, thereby accelerating their growth worldwide [3].

Among the various cell formats used in the automotive industry, the 4680 cylindrical cells have garnered considerable attention. These cells are used in several Tesla models, as well as 4695 and 46120 cells in the new BMW Neue Klasse [4,5]. The 46xx cell features a novel tabless design that improves electrical and thermal performance. This design eliminates the traditional tabs that connect the anode and cathode to the cell's terminals, thereby reducing internal resistance and heat generation during operation. Additionally, the tabless design facilitates better heat dissipation and uniform temperature distribution, which are crucial for maintaining better battery performance and safety during high-power operations [6]. The move towards larger cylindrical cells, such as the 4680, is motivated by the need to enhance energy density and reduce overall cost per kilowatt-hour. Studies have shown that increasing the cell size can significantly improve the volumetric energy density, thereby enabling longer driving ranges and better performance. Moreover, the structural integration of these cells into the vehicle chassis offers additional benefits in terms of weight reduction and structural integrity [7].

Transitioning from the cell level to modules and packs involves understanding and mitigating energy losses at each stage. Energy losses increase as we move from cell-level integration to module-level and finally to pack-level integration due to additional components and interconnections required. These losses can significantly impact the overall efficiency and performance of electric vehicles [8].

To address these challenges, the concept of Cell-to-X (CTX) integration has been developed. CTX eliminates the traditional cell-module-pack structure, allowing cells to be integrated directly into higher-level vehicle components rather than being enclosed in intermediate housings. This reduces redundant structural and functional elements and enables lighter, more compact and energy-efficient designs. The three most widespread strategies are Cell-to-Pack (CTP), Module-to-Chassis (MTC) and Cell-to-Chassis (CTC), of which CTC offers the most significant potential for innovation in EV efficiency and performance [9]. The CTP concept enhances the energy density, efficiency and cost-effectiveness of battery packs by simplifying the system architecture. In traditional designs, cells are first grouped into modules before being integrated into a pack; this modular structure adds weight and material consumption and reduces usable volume. CTP removes the intermediate module stage, integrating cells directly into the pack and thereby increasing both gravimetric and volumetric energy density, reportedly by up to 20% at the system level compared to conventional modular systems [10]. Because the cells are directly connected to the pack's cooling and protective structures, thermal resistance is also reduced, improving heat dissipation and thermal stability. Figure 1 illustrates how CTP designs fill the entire installation space without a module level.

The CTC concept goes a step further, integrating cells directly into the vehicle's load-bearing structure and eliminating the boundary between the battery system and the chassis (Figure 2). Unlike a CTP pack, which can be removed without a significant loss of chassis rigidity, a CTC battery cannot be removed without compromising the chassis's mechanical integrity. Because the cells actively contribute to stiffness and strength, the vehicle's center of gravity is lowered and crash energy can be distributed more efficiently across the structure, improving driving dynamics and crash safety. At the same time, this tight integration complicates repairs and cell replacement and places high demands on manufacturing and quality assurance, since the cells must simultaneously satisfy cooling,

protection and load-bearing requirements using materials such as composites or high-strength aluminum alloys [11].

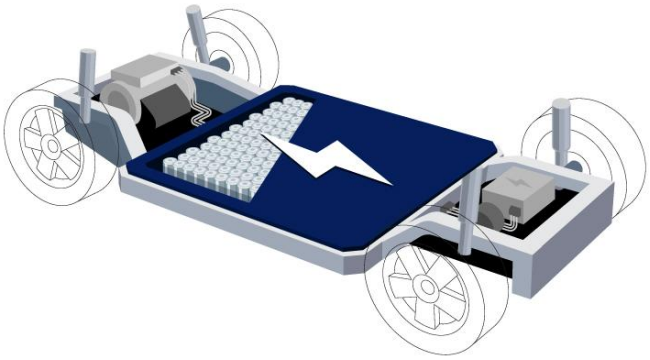


Figure 1. The cells fill the entire installation space of the chassis.

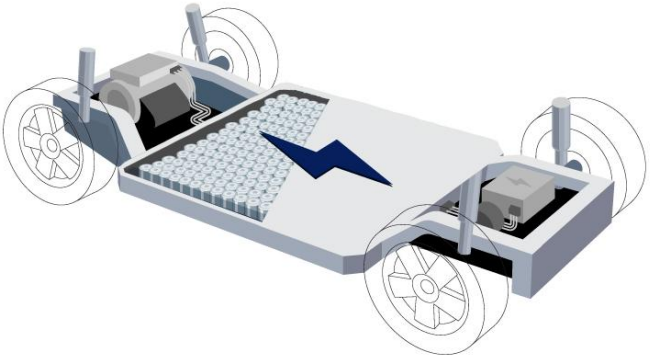


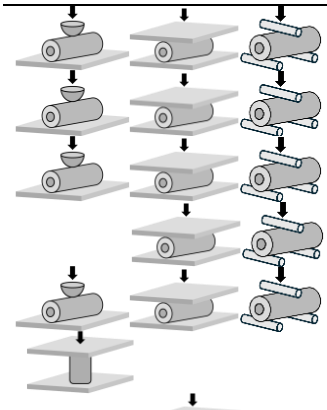
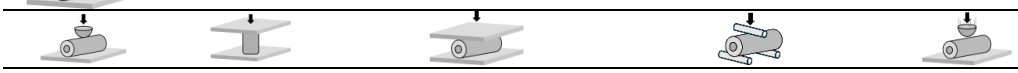
Figure 2. The battery system is already integrated into the chassis.

Additionally, this approach can significantly reduce the complexity and cost of battery packs, providing a competitive advantage in the automotive market [12]. The CTX concept opens the possibility of using cells or modules as part of the vehicle crash structure. This approach allows it to absorb and dissipate crash energy during a collision. By effectively utilizing the inherent strength and rigidity of the battery cells, manufacturers can design vehicles that not only store energy more efficiently but also enhance crashworthiness. This dual functionality can lead to significant weight savings, as the need for separate protection structures is reduced or eliminated and the overall vehicle design becomes more compact and efficient [13,14]. The mechanical characterization of 4680 cells, along with the exploration of structural batteries and Cell-to-X technology, is essential for understanding the full potential of these innovations. Mechanical characterization involves assessing the physical and mechanical properties of battery cells, such as their mechanical strength, durability and response to stress and strain. This information is crucial for ensuring the safety and reliability of batteries under various operating conditions, especially in the context of mechanical stress [15]. These insights can be used to develop new cell housings, cell geometries or materials, thereby realizing the CTX concept**.**

Table 1 provides an overview of previous mechanical abuse tests conducted on cylindrical cells. It is evident that all these tests aimed to deform and damage the cells. However, the objective of this work is to study the elastic deformation range of the cells within the context of the CTX approach, the regime relevant to everyday structural loads, rather than crash-level abuse. In conclusion, the mechanical characterization of 4680 cells, along with the development of structural batteries and Cell-to-X technology, represents a significant advancement in

the field of electric vehicles, with the potential to enhance the performance, safety and affordability of EVs and accelerate the transition to sustainable transportation.

Table 1. Overview of previous studies for cylindrical cells.

Load Case	Loading	SOC [%]	Capacity [Ah]	# Tests	Ref/Year
	Quasi-static	0	45	20	[16]/2012
	Quasi-static	10	2.6	8	[17]/2012
	Dynamic	0	45	30	[18]/2015
	Quasi-static	0–100	2.25	20	[19]/2016
	Quasi-static	0–80	2.25	35	[20]/2016
	Quasi-static	0	2.6	4	[21]/2016
	Dynamic	0/40	2.1/2.5	45	[22]/ 2020
	Quasi-static/ Dynamic	0	2.5	30	[23]/2023
	Dynamic	0/30/60	3.4	34	[24]/2023
	Quasi-static	0–100	2.6/2/1.53	24	[25]/2024
	Quasi-static	30/60	2.9/3.4	32	[26]/2024
	Quasi-static	30/100	23	37	This work
					
Indentation	Radial compression	Axial compression	Three-Point-Bending	Drop weight	

2. Experimental Section

In this section, the methodological framework will be outlined to evaluate the physical and mechanical properties of automotive 4680 lithium-ion cells, focusing on their application as structural batteries in electric vehicles. A series of experimental non-abuse tests will be conducted under various conditions, which include compression tests to evaluate the cells' deformation behavior, durability and safety.

2.1. Specimen

The cells examined in this study are 4680 cylindrical cells. Due to confidentiality issues, it is not possible to obtain original and functional 4680 Tesla cells. As a result, various cell manufacturers available on the market were contacted and samples were ordered. Three different cell manufacturers based in China were selected for comparison. The cell suppliers are Shenzhen Unis Technology (Supplier 1), Shenzhen Vapcell Technology (Supplier 2), and Dongguan Belifine Battery (Supplier 3). All cells are equipped with a cathode made of NMC811 and an anode made of graphite.

The primary objective was to identify structural and electrical similarities between these cells and Tesla's original 4680 cells, which were removed from a deeply discharged Model Y battery system. Because only deeply discharged Tesla cells were available, they could not be used for the tests and were therefore used only for the teardowns. Four cells from each batch were subjected to a series of cycling tests to evaluate their basic

performance characteristics. These tests included initial voltage profiling and capacity measurement to evaluate their similarity to Tesla's known cell specifications. All cells of each batch underwent a standardized cycling procedure according to ISO 12405-4:2018 [27]. After cycling, the cells were torn down in a glovebox model UniLab Pro (MBRAUN, Garching, Germany) to assess their internal structure and materials. Upon comparison, it was observed that the structural design of these cells is remarkably similar to that of Tesla's, with minimal differences noted. All cells were equipped with hexagonal cathode and anode disks attached at the top and bottom. The cathode side consists of small, folded aluminum pieces, while the anode side is made of copper pieces. The torn-down cell structure mirrors the structure of a Tesla 4680 cell. A cross-sectional view of the 4680 cell, illustrating its internal structure and layer arrangement, is provided in Figure 3.

As part of the selection process, the mechanical properties of the cells were analyzed. Accordingly, the connections to the terminals were analyzed and compared with each other. The specifications and characteristics of all cells can be found in Table 2.

Table 2. Datasheet of the Tesla cell and the suppliers 1–3.

Specification	Tesla 4680 [28]	Supplier 1	Supplier 2	Supplier 3
Nominal voltage [V]	3.7	3.7	3.6	3.7
Voltage range [V]	2.5–4.2	2.5–4.2	2.5–4.2	2.75–4.2
Capacity [Ah]	23	23	23	23
Gravimetric energy [Wh/kg]	232–244	233.91	281.66	218.21
Volumetric energy [Wh/L]	622–650	612.25	622.78	640.08
Weight [g]	355	355 ± 7	319 ± 10	≤390

Based on this comparison, Supplier 1 was selected for the main mechanical test program (Cell IDs T1–T40), as it showed the closest overall mechanical and electrical similarity to the original Tesla 4680 cells among the three suppliers evaluated. Its nominal voltage (3.7 V), voltage range (2.5–4.2 V), and capacity (23 Ah) matched the Tesla reference exactly; its gravimetric energy density (233.91 Wh/kg) fell within Tesla's reported range (232–244 Wh/kg), and its terminal connection design most closely resembled that of the Tesla cell (Section 2.1). Information on whether the 40 cells used in the mechanical tests originated from the same production batch as the four cells used for the teardown comparison is not available. This is acknowledged as a limitation, as undetected batch-to-batch variation cannot be ruled out. The results of this study should therefore be understood as characterizing this specific commercial 4680-format cell type (Supplier 1) rather than as generally representative of all 4680 cells on the market, including Tesla's own cells, which could not be obtained for direct mechanical testing.

This cell design features several key structural components that distinguish it from previous battery formats. With a diameter of 46 mm and a height of 80 mm, it offers a larger volume for active material, increasing the cell's energy capacity to 23 Ah, a significant improvement over the previous 21700 cell format.

The separators are longer than the electrodes to wrap around completely, adding safety by preventing short circuits. The outer casing of the 4680 cell is made of nickel-plated steel, known for its corrosion resistance and good electrical conductivity, as well as good thermal conductivity. The top cathode disk is welded to the positive terminal, made of aluminum. The bottom anode disk is mechanically connected to the bottom of the cell housing by crimping. The can has a wall thickness of 0.6 mm, designed to balance mechanical strength and weight. The cell is designed with a pressure relief vent. This venting mechanism is engineered to open in a controlled manner, releasing gases safely to prevent an explosion. The vent is located at the bottom of the cell to direct gases away from the battery system, thereby preventing heat buildup in surrounding cells and components.

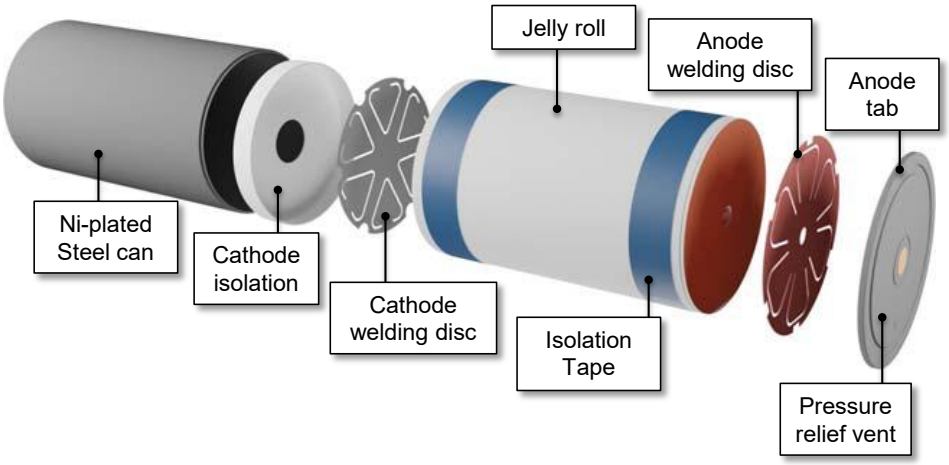


Figure 3. Schematic representation of a 4680 battery cell.

2.2. Experimental Setup

All tests were carried out on a specially developed test stand shown in Figure 4. An electric cylinder model ESBF-BS-80-200-15P (FESTO, Esslingen, Germany) was used as the actuator. The cylinder can reach a maximum speed of 0.7 m/s and has a travel distance of 200 mm and a repeat accuracy of ±0.01 mm. The maximum pressing force is 12 kN. The cell is placed on a horizontal support made of stainless steel. The cell has a surface contact with the support in a range of 60°, and thus, displacement is prevented.

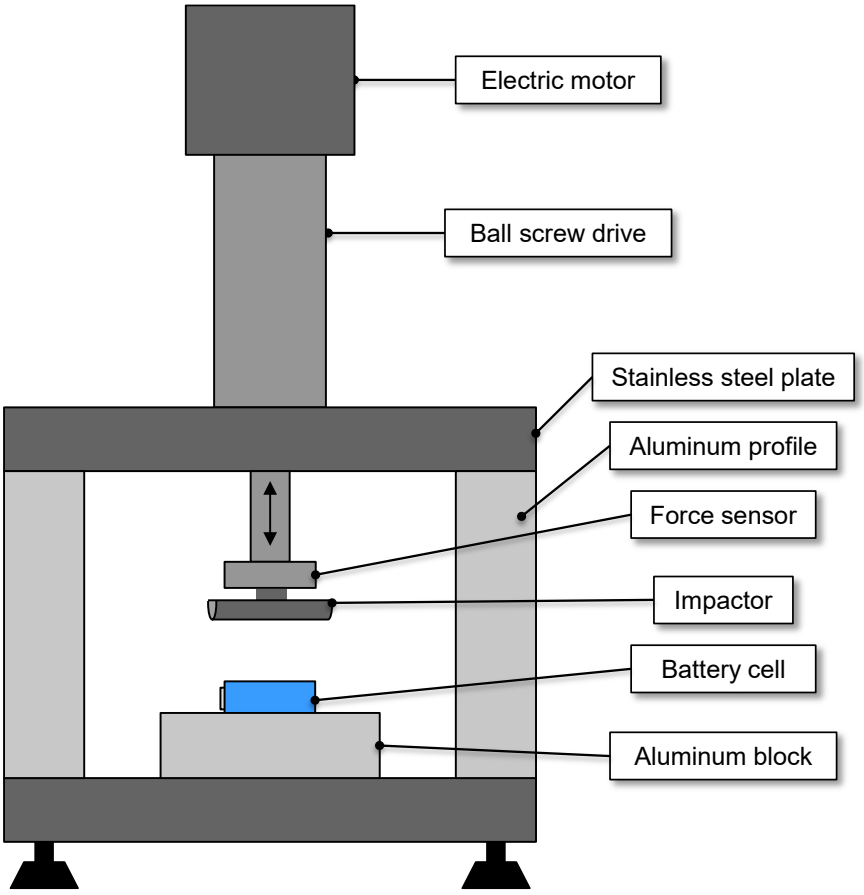


Figure 4. Schematic representation of the test setup.

Special attention was paid to the rigidity of the test system to ensure the most accurate measurement possible. For this reason, 20 mm thick stainless-steel plates were used

as top and bottom plates, which were screwed to extruded aluminum profiles using M12 screws. The cylinder was controlled using the electric motor's own software, which includes integrated control in combination with the measured force. The test system is open on all sides since non-destructive tests are being conducted. Additionally, the test system is placed in a battery testing chamber (BTC), equipped with an exhaust system to minimize air pollution and cell debris in the event of a thermal runaway. The control and regulation were carried out using network communication on a computer. Within the BTC, a thermal camera is placed to monitor the cell, providing a visual indication of heat generation during testing. However, due to the limited accuracy of thermal imaging data, three thermocouples (Type K) are positioned along the cell's axis for more precise temperature measurements, as shown in Figure 5. These sensors are secured with Kapton tape, selected for its high temperature resistance.

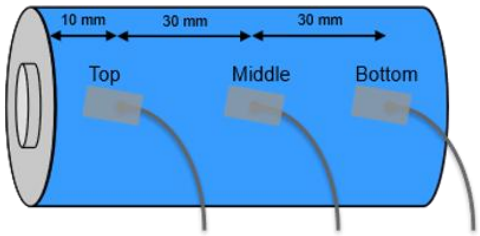


Figure 5. Positioning of the type K thermocouples.

Two different types of impactors were utilized, as illustrated in Figure 6. In setup H, a hemispherical impactor with a diameter of 50 mm is applied to the center of the cell lying flat. The hemispherical test specimen was selected to simulate localized impacts, which ideally do not occur in a CTX approach. This approach therefore represents an extreme case. The center of the cell is used as the point of force application to provide symmetry, ensuring uniform stress distribution. This central position also allows for a consistent and repeatable test setup, minimizing variables in the deformation response and enabling accurate measurement of mechanical properties like stiffness and resilience under compression. Additionally, testing at the center facilitates the evaluation of the cells' structural integrity in their most vulnerable area, as off-center impacts may introduce asymmetric stress distribution, potentially leading to inconsistent test results.

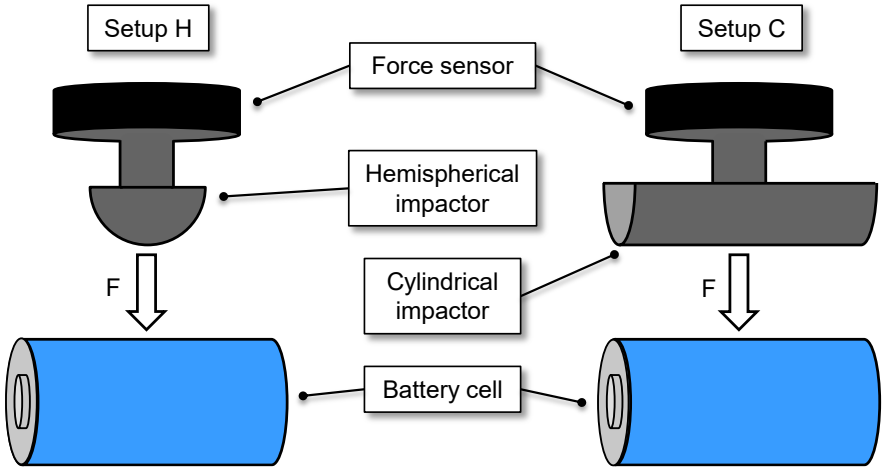


Figure 6. Schematic structure of hemispherical (Setup H) and cylindrical (Setup C) impactors.

In setup C, a long cylindrical impactor with a diameter of 46 mm and a length of 120 mm is used, deforming the cell in the same manner as in setup H, but instead, the contact region forms a line rather than a point. The more relevant setup C represents a scenario

where deformation occurs due to surrounding cells in a vehicle. When the side wall of the vehicle is compressed, forces are transferred from one cell to another, as in the cell-to-chassis concept, simulating the squeezing and interaction between adjacent cells. Another goal is to reduce the potting material surrounding the cells to save weight. By doing so, forces that naturally occur during vehicle operation would be transferred to nearby cells, without compromising the performance of the cells in the absence of the potting material. The goal is to determine the maximum force the cells can withstand without permanent deformation. This allows the cylindrical shape of the cells to be utilized as an advantage, enabling them to function as a structural component in the vehicle chassis. A similar approach can be seen in a patent by BYD, which attempts to achieve maximum packing density and to use a honeycomb structure [29].

Before the tests, the selected cells underwent a preconditioning process based on the ISO 12405-4:2018 protocol, which outlines the procedures for testing the performance of lithium-ion battery packs and systems for electric vehicles. Four cells were connected to a self-engineered cell contact unit, which was equipped with gold-plated pins to reduce contact resistance at the connection points, thereby improving current flow during both charging and discharging processes. The cells were initially charged to 100% SOC using a battery cycler (AMETEK SI-9300R, Berwyn, PA, USA) and placed in a climate chamber (BINDER, Tuttlingen, Germany) set to 20 °C. After a resting phase of 30 min, discharging was performed at a rate of C/3 down to a cut-off voltage of 2.5 V until the current reached a value of C/20. Charging was performed at a rate of C/3 until the cells reached their maximum voltage of 4.2 V, followed by a constant voltage phase until the current dropped to C/20. The cycling process was repeated for 3 cycles. This preconditioning ensures that the cells are in a consistent state for testing and analysis. After the preconditioning process, one cell from each batch was discharged to 0 V to ensure safe handling and reduce the risk of short-circuiting and thermal runaway during disassembly. For the subsequent tests, the cells were charged to 100% SOC and 30% SOC. Since the discharged capacity ΔQ = 16.1 Ah was calculated from the manufacturer's nominal capacity of 23 Ah rather than the cells' actual measured capacity, and the measured capacities of individual cells (obtained from later cycling data) ranged from 20.6 Ah to 22.6 Ah, the true SOC reached by the 30% SOC cell groups is estimated to have ranged from approximately 24.1% to 28.8% (mean ≈ 27.0%) rather than exactly 30%. This deviation does not apply to the 100% SOC condition, which was defined via a constant-voltage charge to 4.2 V and is therefore independent of the cell's actual capacity. We consider this a limitation of the present study and recommend that future work determine cell-specific capacity prior to SOC adjustment.

2.3. Design of Experiments

Design of Experiments (DoE) is a statistical method for planning controlled experiments such that the effects of several factors and their interactions can be estimated efficiently from a minimum number of runs. In a full factorial design, the total number of factor-level combinations (N) is given by $N = L^f$, where L is the number of levels per factor and f is the number of factors.

In this study, a 2 × 2 full factorial design was planned for each impactor geometry. Within each design, the two factors are state of charge (SOC: 30% and 100%) and relative indentation depth (half or full of the geometry-specific onset of plastic deformation identified in preliminary testing, Section 3.2), giving N = 2^2 = 4 factor-level combinations per geometry. Impactor geometry is therefore treated as a between-design variable rather than as a third independent factor: the absolute indentation depths differ between the hemispherical (0.25 mm/0.5 mm) and the cylindrical impactor (0.9 mm/1.8 mm), because they were set relative to the geometry-specific elastic–plastic threshold rather than to a common absolute value. Depth and geometry are thus confounded by design, and a single

orthogonal 2^3 design with three independently varying factors is not applicable. Each factor-level combination was planned with five repeats, and 10 further cells were kept as reserves to account for unforeseen issues during testing. The conditions actually realized are summarized in Table 3.

Table 3. Realised test matrix: impactor geometry, indentation depth and state of charge per cell

Cell ID	SOC [%]	Indentation Depth [mm]	Impactor
T1–T5	30	0.5	Hemispherical
T6–T8	100	0.25	Hemispherical
T9	30	0.25	Hemispherical
T11, T12, T13, T15	30	0.5	Hemispherical
T16–T19	100	0.25	Hemispherical
T21–T25	30	0.9	Cylindrical
T26–T30	30	1.8	Cylindrical
T31–T35	100	0.9	Cylindrical
T36–T40	100	1.8	Cylindrical

For the cylindrical impactor, the planned design was realized in full: each of the four factor-level combinations was tested with five cells (T21–T40), giving 20 tests. For the hemispherical impactor, it was not. Cell T10 was used for the preliminary tests described in Section 3.2, the tests planned as T14 and T20 were not carried out, and cells T13, T15 and T16 are reserve cells substituted for tests of the original matrix that could not be completed; the hemispherical series therefore comprises 17 rather than 20 tests. More importantly, an audit of the individual test records against the measured indentation depth and the cell voltage logged immediately before each test showed that the two factors were not varied orthogonally in this series: nine tests were performed at 30% SOC with 0.5 mm indentation, seven at 100% SOC with 0.25 mm indentation, one at 30% SOC with 0.25 mm (cell T9), and none at 100% SOC with 0.5 mm. State of charge and indentation depth are therefore almost completely confounded for the hemispherical impactor, one factor-level combination is empty and a second contains a single specimen. Consequently, no analysis of variance is reported for the hemispherical series; all hemispherical results in Section 3.3 are presented descriptively and are to be understood as exploratory. The hemispherical tests were carried out in two campaigns between which the reference position of the actuator was changed, and are therefore reported separately by campaign. For the same reason—geometry being confounded with absolute indentation depth, contact area and the geometry-specific reference threshold—the comparison between the two impactors does not represent a controlled factor effect either. It is reported as a descriptive, exploratory comparison only, and no statistical inference regarding a geometry main effect or a geometry × depth interaction is drawn from it. All confirmatory statistical analysis is conducted within the cylindrical series.

The indentation depths were set to 0.5 mm and 0.25 mm for the hemispherical impactor and to 1.8 mm and 0.9 mm for the cylindrical impactor. The full depths of 0.5 mm and 1.8 mm were selected with a margin below the onset of plastic deformation identified in the preliminary screening described in Section 3.2; as Section 3.5 shows for cell T36, this does not guarantee identical behavior across all individual cells. The half depths of 0.25 mm and 0.9 mm were selected to cover a distinctly lower stress level, allowing the influence of the mechanical load on voltage and capacity to be examined at two magnitudes. The SOC values were set at 30% and 100%, representing typical operating conditions and a worst-case scenario. A 0% SOC was not considered, as it was assumed that minimal short-term deformation at this state would not significantly affect the voltage or capacity, given the low energy stored within the cell.

2.4. Elastic Deformation

Understanding the distinction between elastic and plastic deformation is essential for evaluating the mechanical resilience of battery cells in the context of Cell-to-X integration. Within the elastic region, the material deforms in direct, reversible response to the applied load and returns to its original shape once the load is removed; beyond the elastic limit, or yield point, the material enters the plastic region, where permanent deformation occurs. As this study is a non-destructive characterization, the aim is to identify the elastic range of the cell in which no measurable degradation of function or structure occurs—the usable mechanical load capacity relevant to a Cell-to-Chassis approach—rather than to predict the cell's mechanical response from first-principles contact theory. The elastic–plastic transition thresholds used in this study (Section 3.2) were therefore determined empirically through stepwise indentation testing with continuous force-displacement logging, rather than derived analytically, since the cell's layered jelly-roll structure and thin-walled casing depart substantially from the homogeneous, isotropic solid assumed in classical contact mechanics models such as Hertzian theory.

This approach not only facilitates the evaluation of cell stiffness but also provides critical data on the mechanical resilience of the cells when integrated into the CTX concept. The aim is to understand how the cells behave under conditions that closely mimic real-world stresses they would encounter during normal usage. Moreover, the inclusion of factors like SOC and contact area aligns with findings that these parameters significantly influence the mechanical behavior of cells. SOC has been noted to affect the internal pressure and potential for thermal runaway during impact [30]. Similarly, the contact area impacts the distribution of stress across the cell, influencing the likelihood of localized damage [31].

3. Results and Discussion

The following section presents and analyzes the mechanical test results obtained from quasi-static compression experiments. Building on the design of experiments and structural comparison discussed previously, the objective is to quantify the mechanical response of these cells under different loading conditions relevant for structural integration in electric vehicles.

This analysis is significant in the context of the CTX concept, where battery cells are realized as load-bearing elements within the vehicle chassis. The findings in this section aim to identify the limits of elastic deformation and to assess the cells' potential to endure mechanical stress without permanent damage or capacity loss.

3.1. Preconditioning

As described in Section 2.2, each cell underwent three charge–discharge cycles according to the ISO 12405-4:2018 protocol prior to testing. Figure 7 illustrates the resulting voltage and current profiles over time for the tested Cell T2, confirming consistent and reproducible charge–discharge behavior.

The process of preconditioning is essential to ensure the cell's performance stabilizes before main testing, ensuring consistent capacity and electrochemical behavior over time. Preconditioning typically helps in formatting the electrodes, stabilizing the solid electrolyte interphase (SEI) and improving cycle life predictions.

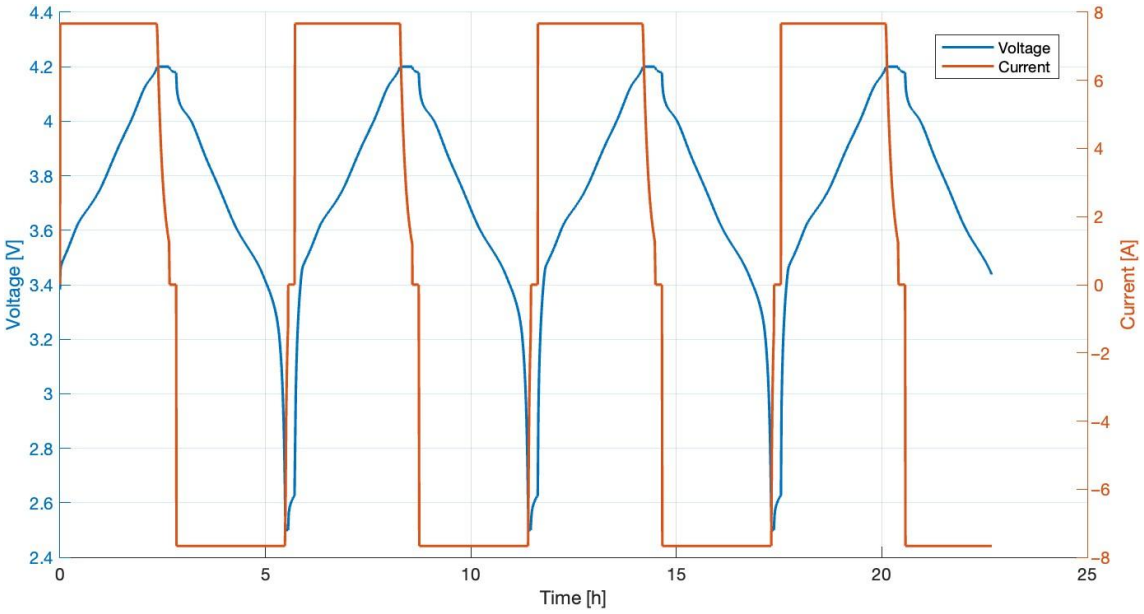


Figure 7. Voltage and current profile after preconditioning of cell T2.

After the preconditioning phase, the cells are charged again before being adjusted to the desired state of charge. For the execution of the experiments, it is therefore necessary to precisely set the battery cells to 100% and 30% SOC. The tested cells have a total capacity of 23 Ah, which corresponds to 100% SOC. To reach an SOC of 30%, the cell is discharged until only 30% of the charge remains. The discharge process begins from a fully charged state, corresponding to the maximum capacity of 23 Ah. Thus, the amount of charge to be discharged is 16.1 Ah. This method was chosen because the suppliers did not provide any OCV curves for the cells.

The cells are discharged using a constant current of C/3, which corresponds to a discharge current of 7.67 A. The time required to discharge the cell to 30% SOC is calculated using the following equation

$$t = \frac{\Delta Q}{I_e} = \frac{Q_{100\%} - Q_{30\%}}{I_e} \quad (1)$$

where the discharged capacity is ΔQ = 16.1 Ah and the discharge current is I_e = 7.67 A. This results in a discharge time of t = 2.1 h (2 h and 6 min) to reach 30% SOC.

Following the discharge process, a one-hour relaxation phase is implemented to ensure that the cell voltage stabilizes and the targeted SOC of 30% is accurately achieved. This procedure ensures consistent and reproducible initial conditions for the subsequent mechanical and electrical tests.

3.2. Preliminary Tests

It should be noted that the loading conditions investigated in this study are intended to represent the mechanical stresses a cell may experience as a load-bearing structural element during normal vehicle operation, such as road-induced vibration, thermal-expansion-driven contact pressure between adjacent cells, or assembly preload, rather than crash-level loading. This distinction is consistent with established automotive battery test standards, which separate long-term operational vibration testing (e.g., SAE J2380, based on road-load measurements) from dedicated crash-related mechanical tests (e.g., "contact force at vehicle crash" in ISO 12405-4, ECE R100.02) [27,32,33]. The elastic, non-destructive regime examined here is therefore relevant to assessing whether a cell can reliably serve as a structural element under everyday operational loads. Crashworthiness, which involves substantially larger, destructive deformations, is addressed separately by the

abuse-testing literature summarized in Table 1. A quantitative link between the tested indentation depths and specific operational load magnitudes (e.g., derived from vehicle-level vibration data, finite-element simulation, or OEM structural specifications) was beyond the scope of this study, as such data are not publicly available for Cell-to-X architectures, and is identified as an important direction for future work.

After the completion of the preconditioning phase, preliminary tests were conducted to identify the onset of plastic deformation under compressive load. For each impactor type, a single fully charged cell at 100% SOC was tested using a stepwise procedure: The indentation depth was increased incrementally, and for each step, the complete loading and unloading force–displacement curve was logged continuously, with the cell inspected for visible casing deformation before proceeding to the next, deeper step.

For the cylindrical impactor, this procedure confirmed that up to an indentation depth of 1.8 mm, the logged curves returned to the initial contact position within measurement resolution (residual displacement ≤ 0.1 mm), with no visible casing deformation observed. For the hemispherical impactor, a re-examination of the logged curves showed that in the first screening run, the actuator had been started approximately 0.4 mm above the point of first contact, so that the nominal 0.5 mm stroke produced only about 0.1 mm of actual indentation at a peak force of 96 N. The screening was therefore repeated with the start position set at the contact point. Under these conditions, a 0.5 mm indentation produced peak forces of 567 N and 707 N with no visible casing deformation, whereas a subsequent indentation to 0.7 mm produced a peak force of 963 N together with a residual displacement of ≈0.14 mm and a visible plastic indentation of the casing. The depths of 0.5 mm and 1.8 mm used in the main experiments were therefore selected with a margin below this empirically identified onset in the screening cells, rather than as universally guaranteed thresholds of reversible deformation. As Section 3.5 shows, individual cells can still exhibit localized plastic deformation at these depths.

In addition to the full depths, half-depth conditions of 0.25 mm and 0.9 mm were included in the DoE not as separate elastic-limit determinations, but as a deliberately lower-stress comparison condition to examine whether cycling-induced aging effects differ between the two mechanical stress levels.

To further characterize the loading-unloading behavior, the dissipated energy (area enclosed by the loading and unloading force-displacement curves) was calculated for the available logged tests. For the cylindrical preliminary-screening cell at 1.8 mm (near-zero residual displacement), 52.5% of the input mechanical work was dissipated. For cell T12 at 0.7 mm (0.14 mm residual displacement), 34.6% was dissipated. And for cell T36 at 1.8 mm (0.46 mm residual displacement, Section 3.5), 58.0% was dissipated. As dissipated energy did not scale cleanly with residual displacement across these tests, we attribute a substantial fraction of the measured hysteresis to system-level effects (actuator backlash, sensor response lag) rather than to the cell alone, and therefore consider residual displacement the more direct and reliable indicator of plastic deformation in this setup.

3.3. Mechanical Cell Loading

Following the preliminary tests, the analysis of the mechanical loading of the cells is carried out in the form of compression tests. The objective of these tests is to systematically examine the force–displacement behavior at defined indentation depths to characterize the mechanical stability and response of the cells under various loading scenarios. This subsection focuses specifically on Setup C using the cylindrical impactor to analyze the force progression over displacement for a specific group of cells.

Figure 8 shows the force–displacement curves of a cell group, which was tested using a cylindrical impactor. The cells were compressed to a maximum indentation depth of 1.8 mm, with a peak force of 5.19 kN recorded, demonstrating the structural load-bearing

capacity of the cell. This value provides important information for the design of mechanical safety features in battery systems, particularly regarding external mechanical influences such as those occurring in crash scenarios. The observation that the force curves remain consistent up to the maximum indentation depth indicates that the cells exhibit a homogeneous mechanical response. Furthermore, the force progression shows a continuous increase with indentation depth, suggesting an increasing resistance of the cell to mechanical loading. The different curves in the graph represent the results of multiple cells and reflect a high reproducibility of the tests. Building on the analysis of the force–displacement curves obtained from the compression tests, the following section provides a detailed description and discussion of the temperature, voltage and force behavior of cell T30 during a mechanical load test.

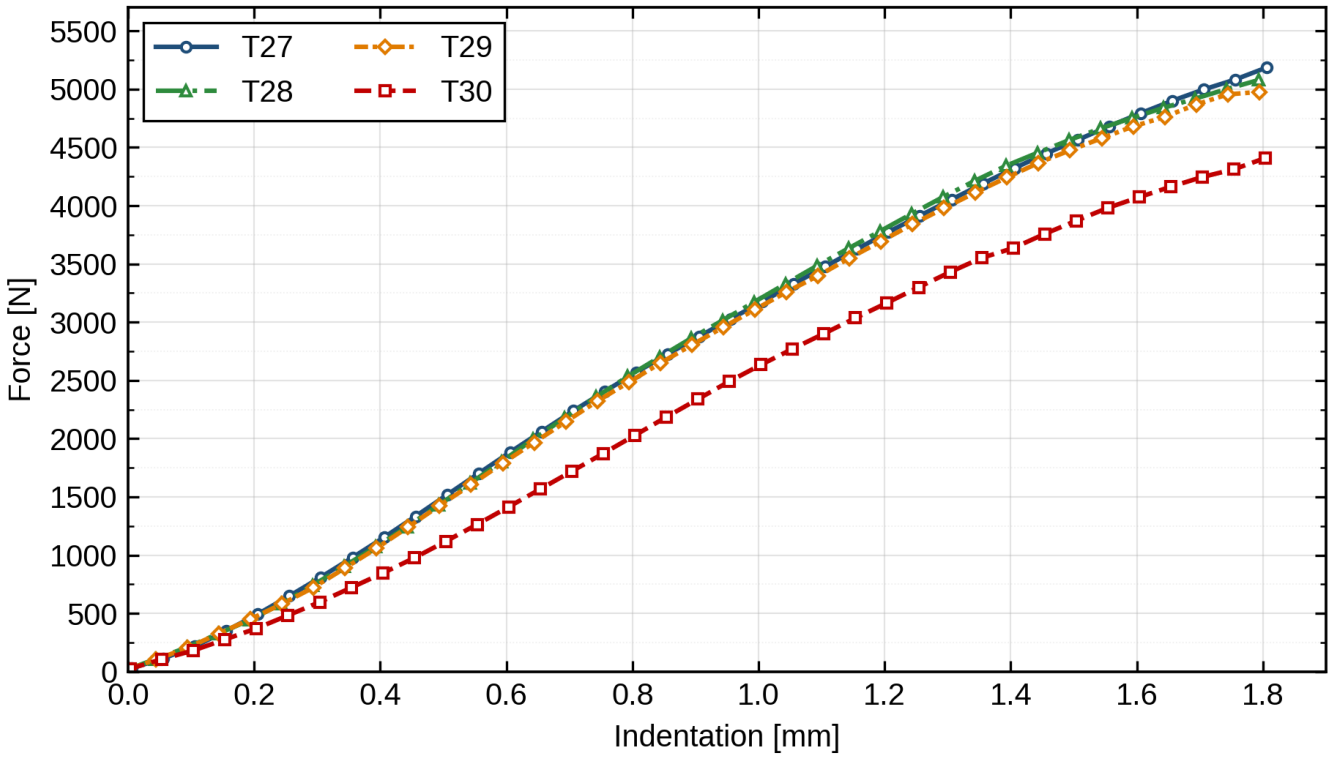


Figure 8. Force progress of a cell group with Setup C, 30% SOC and 1.8 mm indentation.

Figure 9 illustrates the simultaneous measurements of temperature, force, and voltage over time, offering insights into the cell's behavior under compressive loading.

The upper plot displays the temperature profile, with individual readings taken from three sections of the cell. A minimal temperature increase of approximately 0.1 °C is observed, with the red line marking the time point of maximum force application. However, this increase cannot be directly attributed to the mechanical load, as it falls within the measurement tolerance and shows no systematic correlation with the applied force. The overall temperature stability throughout the test period indicates that heat generation due to compression was negligible. This suggests that the mechanical test did not cause any significant local heating of the cell components, which speaks to the thermal stability of the cell.

The middle plot presents the force progression over time. The applied force reaches a well-defined maximum before returning to zero. The curve follows a symmetrical pattern, reflecting the controlled application and release of mechanical loading. No effect on the previously described temperature or voltage curves is observed following force release. This suggests that the mechanical loading did not result in any lasting structural damage or significant changes in the cell's chemistry. The symmetrical force curve

without abrupt deviations further confirms the precision of the test setup and the reliability of the experimental methodology.

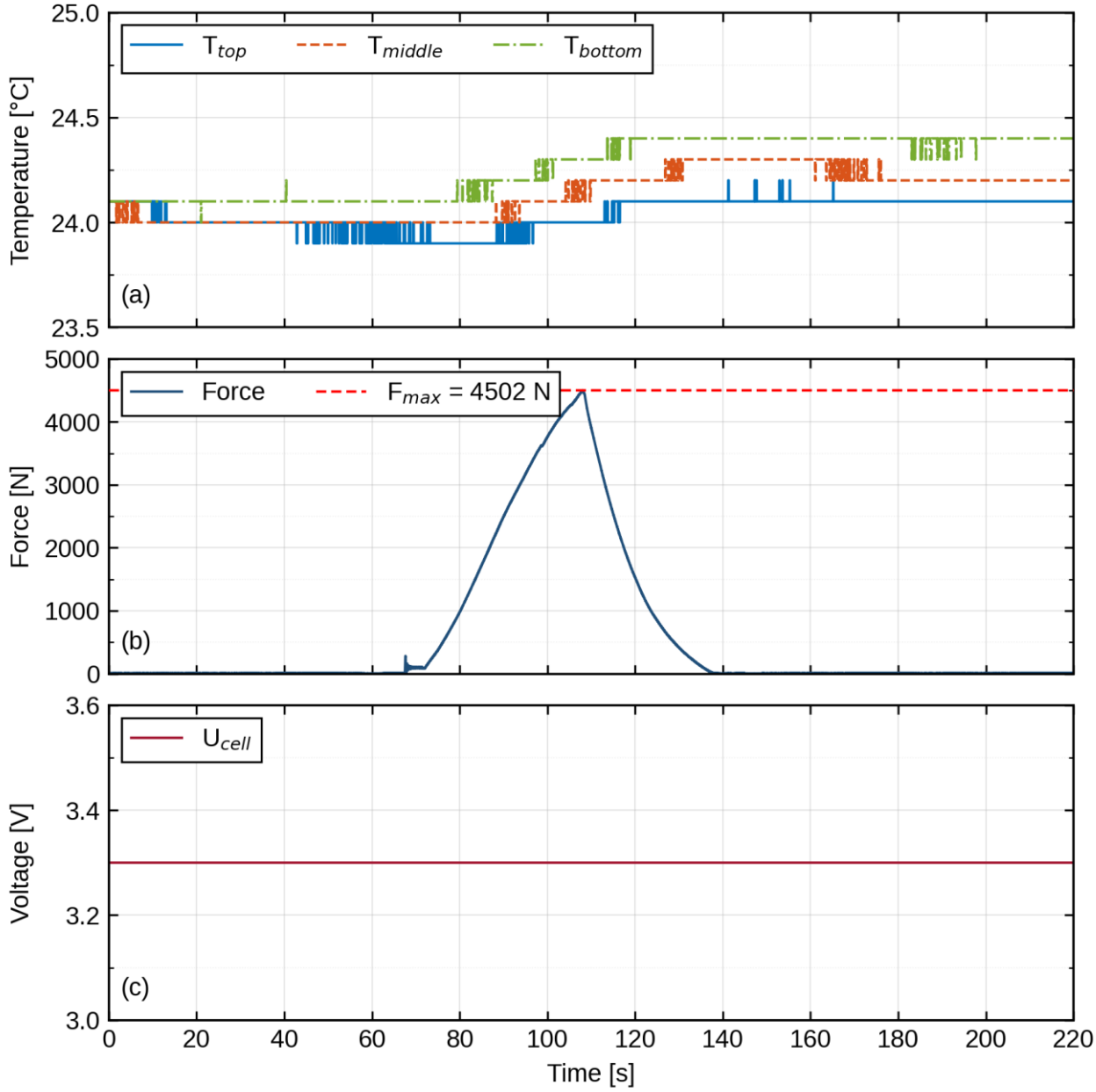


Figure 9. Temperature, force and voltage of cell T30 during loading (30% SOC, 1.8 mm, cylindrical impactor): (**a**) cell temperature at three positions; (**b**) applied force; (**c**) cell voltage.

The lower plot shows the cell's voltage over time. The voltage remains constant at 30% SOC throughout the entire test, with no significant deviation. This shows that the mechanical stress applied to the cell, even at maximum indentation depth, produced no immediate, detectable effect on its electrical integrity or voltage level. Stable voltage and surface temperature during loading provide no immediate evidence of an internal short circuit. However, they do not rule out more subtle effects such as localized separator damage, a soft short circuit, or an increase in internal resistance. This would require dedicated diagnostics, such as DC resistance, electrochemical impedance spectroscopy (EIS), self-discharge, or relaxation-voltage measurements before and after loading, which were not performed in this study.

Figure 10 shows the mean maximum forces measured with the hemispherical impactor, separated by test campaign. Because state of charge and indentation depth are

confounded in this series and one factor-level combination is not populated (Section 2.3), these values are reported descriptively, and no factor effects are inferred from them. The complete set of measurement results is compiled in Appendix A: Table A1 lists the number of tests, mean, standard deviation, coefficient of variation and 95 % confidence interval for every group, and Table A2 reports the individual peak force of each single test.

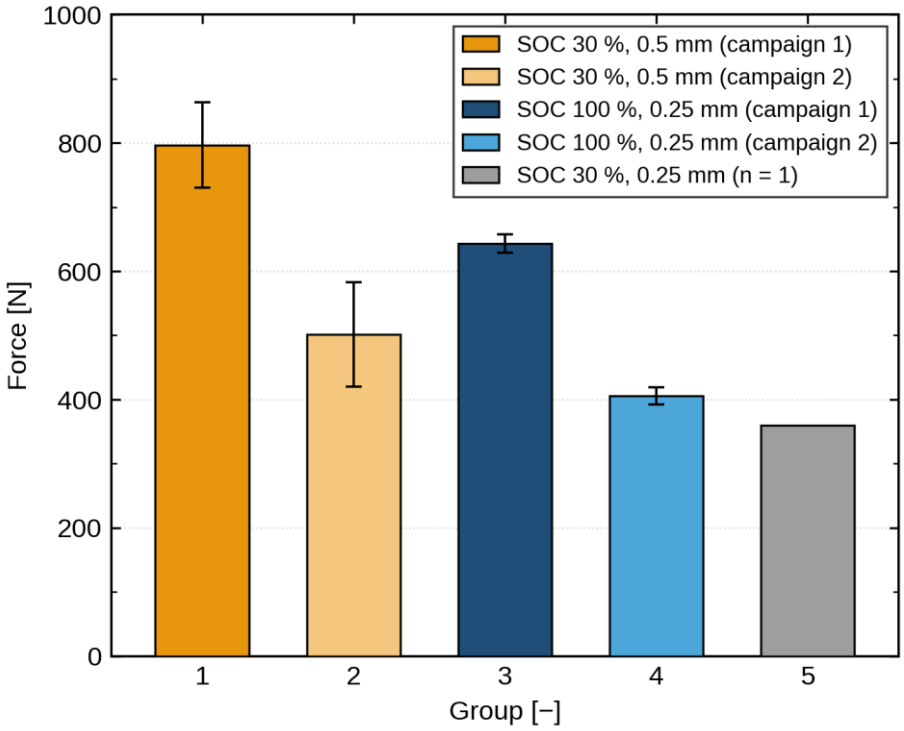


Figure 10. Mean maximum forces of the hemispherical impactor tests by group and test campaign; error bars denote one standard deviation. Group 5 contains a single specimen.

Figure 11, in comparison, shows the average maximum forces measured with the cylindrical impactor. A notable observation is the clear dependence of the maximum force on both the indentation depth and the impactor geometry. The cylindrical impactor generally generates higher forces, which can be explained by the larger contact area and the resulting distribution of mechanical stress across the cell structure. Furthermore, cells tested at 100% SOC consistently exhibit higher maximum forces than those tested at 30% SOC. This can be attributed to the increased mechanical stiffness of the cell structure at higher charge levels. This SOC-dependent stiffening is consistent with prior quasi-static indentation studies on 18650 cylindrical cells, which likewise report increasing peak force and structural stiffness with increasing SOC, attributed to lithiation-induced internal stress and volumetric expansion within the jelly roll [19,20]. A similar trend has also been reported under dynamic and higher-SOC compression loading [24,26], suggesting that the effect persists across loading rates and cell formats. To formally assess the statistical significance of these observations, a two-way analysis of variance (SOC × indentation depth) was conducted for the cylindrical impactor, for which the 2 × 2 design was realized in full with five replicates per combination (n = 20). Both SOC ($F(1,16) = 49.79$, $p < 0.001$) and indentation depth ($F(1,16) = 361.16$, $p < 0.001$) had highly significant effects, with a significant interaction ($F(1,16) = 39.62$, $p < 0.001$). The SOC-dependent increase in peak force was markedly larger at 1.8 mm (5111.8 N at 30% SOC versus 7917.2 N at 100% SOC, 95% CI [4443, 5780] and [6996, 8838], respectively) than at 0.9 mm (2441.2 N versus 2601.2 N, 95% CI [2324, 2559] and [2372, 2830]). The model assumptions were verified: homogeneity of variances across the four factor-level combinations is supported (Levene's test, W

= 1.31, $p = 0.305$), and independence is ensured by design, as each observation corresponds to a separate, previously untested cell. Normality of the residuals is rejected (Shapiro–Wilk, W = 0.847, $p = 0.005$), which is expected given the strong increase in the residual scatter with force level visible in Table A1. The analysis was therefore repeated as a distribution-free permutation ANOVA with 10,000 permutations, which reproduced all three effects ($p \leq 0.0002$ for SOC, depth and their interaction); the conclusions above are thus not an artifact of the normality assumption. No analysis of variance is reported for the hemispherical impactor, for the reasons given in Section 2.3. Comparing the two impactor geometries at matched relative depth, peak forces differ by a factor of roughly three to ten (for example, 2441 N versus 796 N at 30% SOC and half of the geometry-specific threshold; Table A1). As geometry is confounded with absolute indentation depth, contact area and the geometry-specific reference threshold, this comparison is descriptive and exploratory; the magnitude of the difference is consistent with the substantially larger contact area of the cylindrical impactor, but no statistical test of a geometry effect is reported.

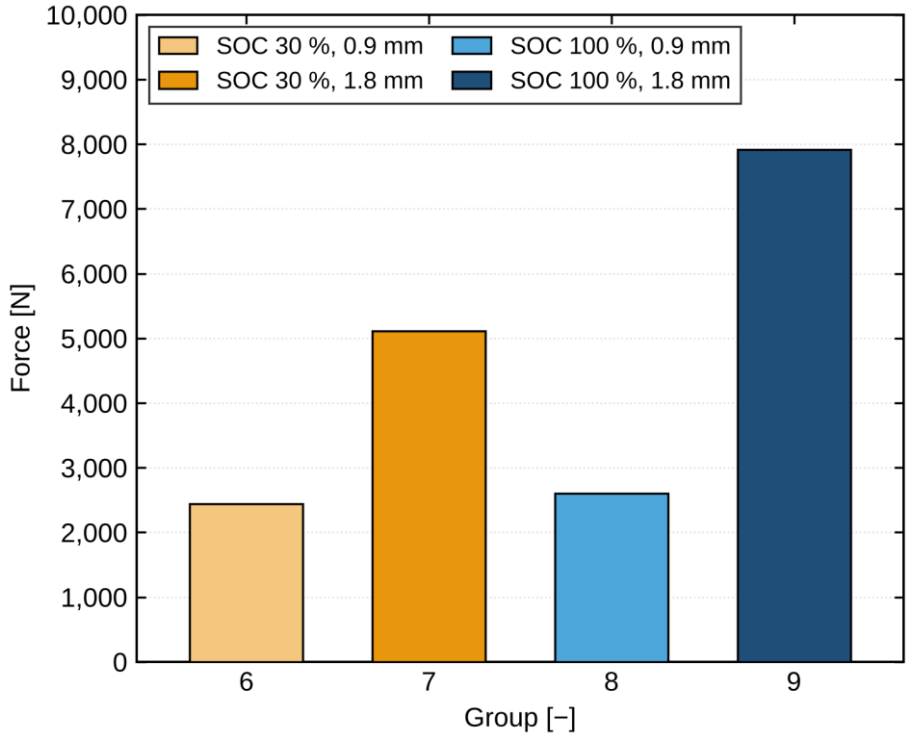


Figure 11. Representation of the maximum average forces of all cylindrical impactor tests.

3.4. Cyclic Cell Aging

This section presents and analyzes the results of the cyclic aging tests performed on the investigated cells. For each cell group, at least one representative cell was selected that reflects the respective test conditions. In addition, one mechanically untested reference cell (T48) was included in the cycling process to enable a comparison of the capacity loss between the mechanically tested cells and an unstressed cell. All cells were subjected to a cycling program of 150 charge and discharge cycles under defined conditions. Figure 12 presents the capacity progression of the reference cell T48. The upper subplot illustrates the absolute charge capacity over all cycles, while the lower subplot shows the percentage change in capacity per cycle. At the beginning of the cycling process, the cell exhibited a charge capacity of 21.22 Ah. After 126 valid cycles, the capacity had decreased to 20.65 Ah, corresponding to a total change of −2.69%.

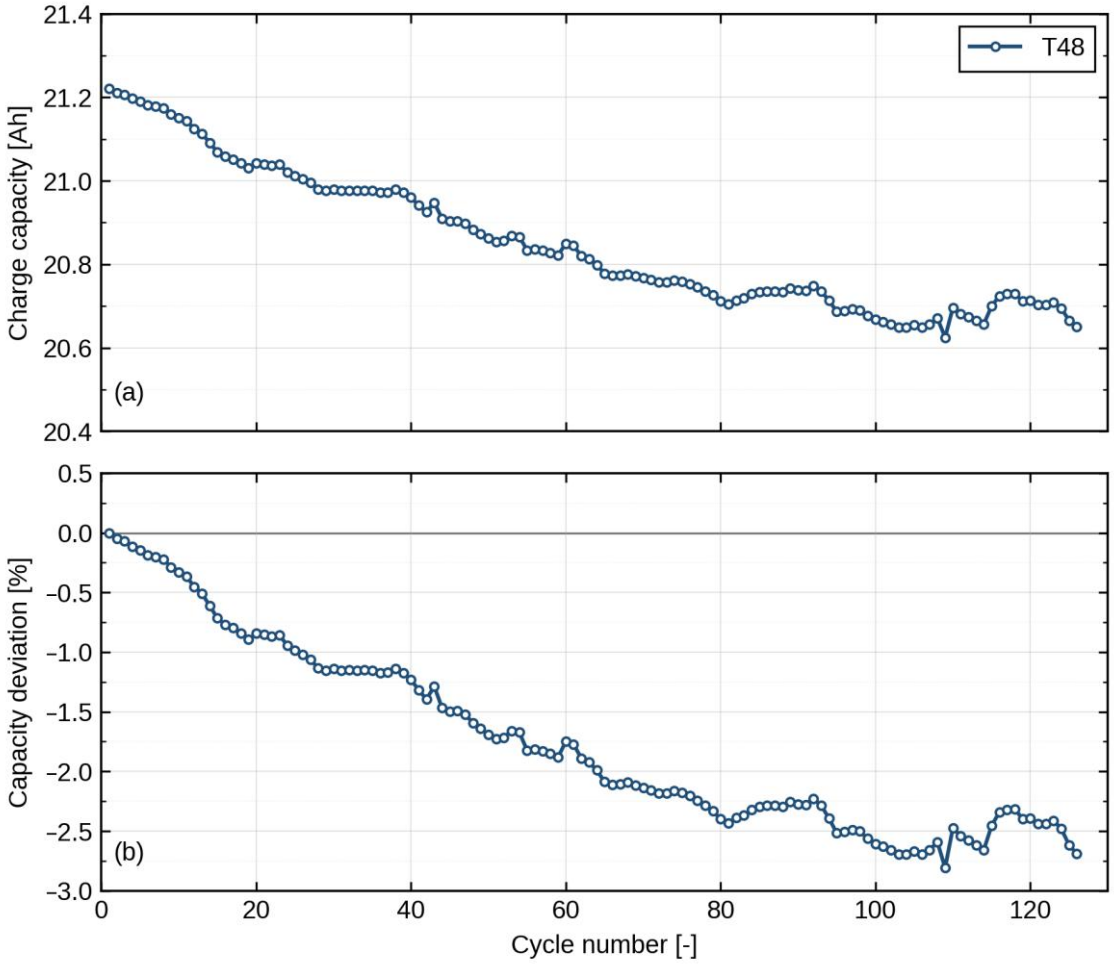


Figure 12. Charge capacity progression over all cycles (**a**) and capacity deviation (**b**).

The curve in the upper subplot reveals a nearly linear decrease in capacity over the cycles, indicating a consistent aging mechanism. There are no abrupt drops or significant fluctuations, highlighting the homogeneity of the cell and the stability of the cycling conditions. This suggests that the internal structure and chemistry of the cell were only minimally affected by the charge and discharge cycles, which is typical for an untested reference cell. The curve in the lower subplot emphasizes the gradual yet minor decline in overall capacity. Variations in the percentage change remain minimal and within the measurement tolerance, demonstrating the consistency of the data and the precision of the test setup. The slight reduction in total capacity, only 2.66% over 120 cycles, demonstrates the high robustness of the reference cell under the given conditions. Based on these values, Figure 13 presents a visualization of the percentage change in charge capacity along with the corresponding standard deviation. The figure displays a boxplot representation of the percentage change in charge capacity during the cycling of the reference cell. The median is close to zero, confirming the minimal change in capacity already evident from the previous results. The distribution of the data points is extremely narrow, and the calculated standard deviation is only 0.07%. This low variability highlights the high stability of the reference cell throughout the test period. Individual outliers shown in the figure also lie within a very tight range and have minimal influence on the overall trend. The small standard deviation and narrow value range in the boxplot demonstrate that the reference cell maintained consistent performance throughout the charge and discharge cycles. The outliers visible in the plot may be attributed to minor measurement

inaccuracies or short-term effects such as charge efficiency losses but are negligible in the context of the overall cell stability.

This behavior is characteristic of cells not subjected to additional mechanical stress, where degradation primarily results from chemical aging of the electrodes and electrolytes. The linear trend suggests the absence of sudden degradation events, which could otherwise be triggered by mechanical influences or elevated temperatures. Compared to the tested cells from other groups that underwent both mechanical loading and cyclic aging, the reference cell, as expected, exhibits a lower degree of capacity degradation. This difference enables a quantification of the additional impact of mechanical stress on the cells and provides insights into the interaction between mechanical and chemical aging processes.

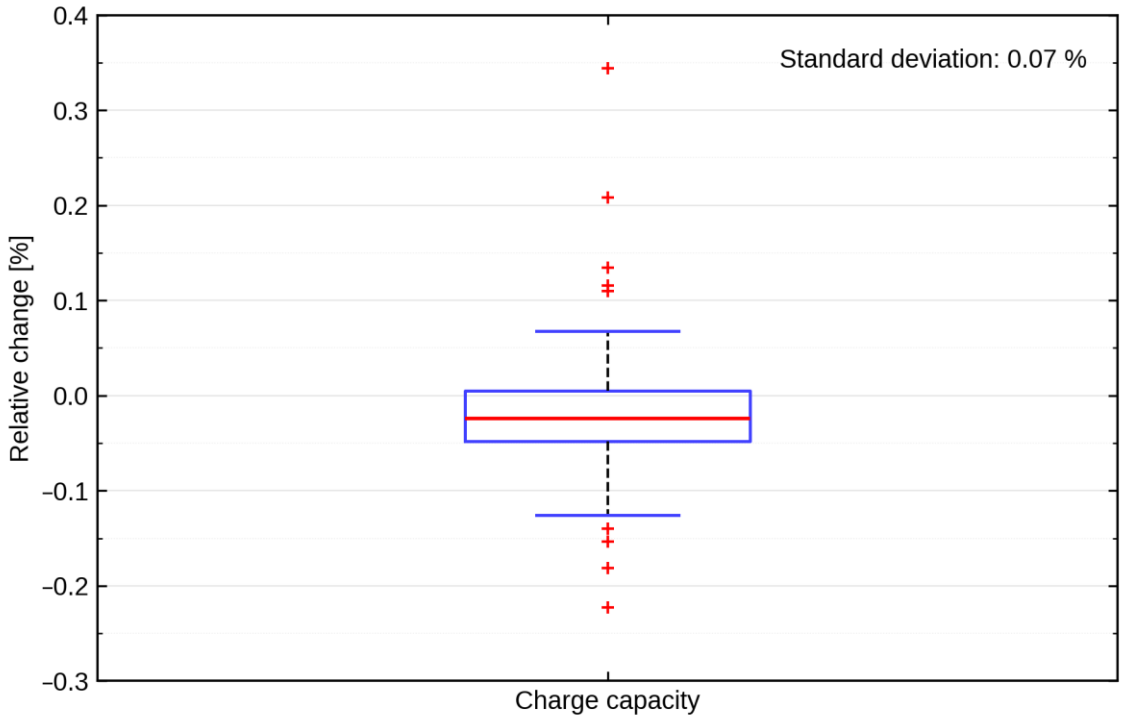


Figure 13. Standard deviation of the charge capacity for the cell T48.

When compared to the results of mechanically stressed cells, the importance of the reference cell as a control becomes evident. The near-perfect stability of the reference cell underscores the additional effects that mechanical stress can induce. It therefore serves as an essential benchmark for evaluating aging mechanisms in stressed cells. Figure 14 illustrates the progression of the charge capacity of eight different cells from various cell groups over the course of 150 cycles.

Compared to the reference cell T48, which exhibited a total capacity change of −2.69% over its 126 valid cycles, the cells shown in the graph also display only minor changes in capacity over the cycles for which a valid record exists. Cell T9 stands out in particular, showing an above-average capacity loss of −7.91% over 62 valid cycles, the largest degradation among all cells with a usable record. The remaining cells with a usable record exhibit losses between −1.82% and −4.09%.

Some cells show gaps and fluctuations in the capacity record during cycling. These originate from aborted cycles. A re-audit of the raw cycler records identified the cause: the interruptions are almost exclusively over-temperature cut-offs of the cell tester. The peak cell temperature reached during cycling is the single discriminator between cells with an essentially complete record and cells with a heavily fragmented one. Every cell that reached 50.0 °C lost the majority of its cycles, and every cell that remained below 49.5

°C completed nearly all of them (Table 4). Interruptions of the recording longer than five minutes, which would indicate a power failure of the test bench, were not found; the attribution to power failures made in the previous version of this manuscript is therefore withdrawn. Affected cycles recorded only a partial charge and were excluded from the evaluation; they are shown as dashed line segments in Figure 14.

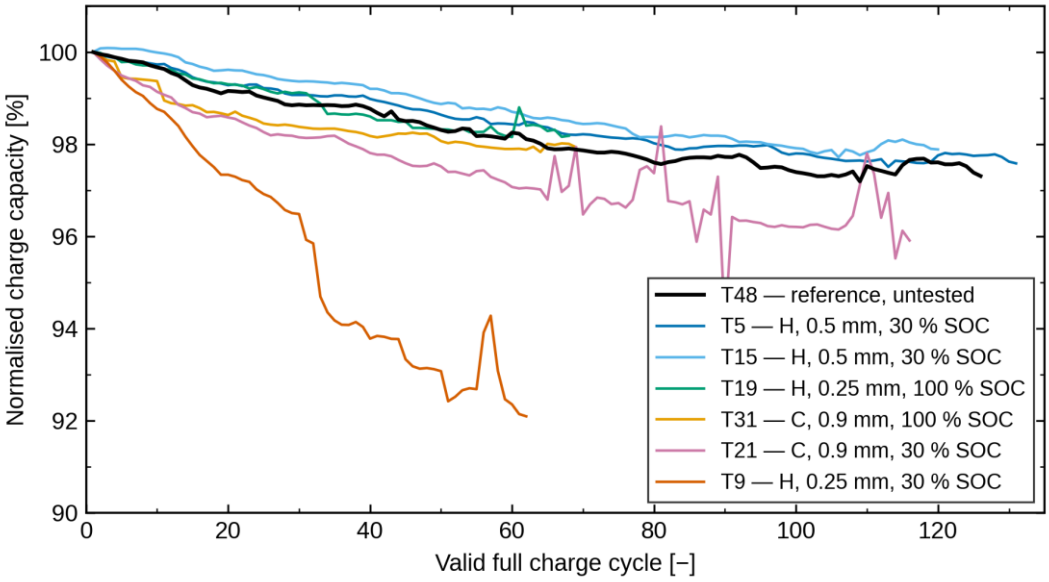


Figure 14. Normalized charge capacity over the valid full charge cycles for all cells with a usable record.

A cycle was counted as valid only if its charge phase started from a completed discharge (cell voltage below 2.75 V), terminated at 4.2 V with the constant-voltage cut-off current of 1.5 A of the cycler, and delivered more than 10 Ah of charge throughput; a cycle whose charge capacity fell below 85% of that of the preceding valid cycle was discarded as physically implausible. Applying this criterion consistently to all records changes the picture for the two cells cycled after the deepest cylindrical indentation. Cells T27 and T36 yield only two and four valid cycles, respectively, rather than the 22 and 27 reported previously, because the remaining charge phases were incomplete. The capacity-loss values previously stated for these two cells are therefore withdrawn: no statement regarding the aging behavior of the 1.8 mm conditions can be made from the present data. This is a limitation of the cycling campaign and not evidence of degradation, as the following comparison shows. Because the number of valid cycles differs substantially between cells, absolute capacity losses are not directly comparable; Table 4 therefore additionally reports the capacity loss normalized to 100 valid cycles.

On this normalized basis, the mechanically loaded cells with a usable record lose between 1.82% and 2.85% per 100 valid cycles, compared with 2.03% for the unstressed reference cell T48, with cell T9 the sole outlier at 13.57%. Two further limitations must be stated. First, the number of interrupted cycles is not related to the severity of the mechanical loading: cell T9, which was subjected to the mildest condition of the entire program (0.25 mm, hemispherical), lost 199 of 261 cycles, whereas cells T5 and T15, loaded to twice that depth, completed almost all of theirs. The loss of cycles tracks the peak cell temperature, not the mechanical load. Second, the reference cell was cycled at a peak temperature approximately 10 K lower than any mechanically loaded cell (40.5 °C versus 47.6–50.2 °C), indicating that the thermal boundary conditions were not uniform across the cycler channels. This is a confounding factor for the reference comparison that is independent of the mechanical question. Given that only one or two cells per condition underwent cycling and only a single unstressed reference cell was available, cell-to-cell variation cannot be statistically separated

from any potential effect of the prior mechanical loading. These results should therefore be interpreted as exploratory observations, consistent with the possibility that the applied mechanical loads did not substantially accelerate capacity fade, rather than as conclusive evidence of this. Confirming this would require replicate cycling of multiple cells per condition, multiple reference cells and uniform thermal boundary conditions, which was not feasible within the scope of this study due to limited test-channel availability and time constraints.

Table 4. Cycle-count data completeness, cause of the interrupted cycles and resulting capacity loss for the cells included in the aging analysis. n.d. = not determinable, too few valid cycles.

Cell ID	Condition	Attempted Cycles	Valid Cycles	Aborted (Over-Temp.)	Capacity Loss	Loss/100 Cycles	T_max [°C]
T48	Reference (mechanically untested)	127	126	0	−2.69%	2.03%	40.5
T5	30% SOC, 0.5 mm, H	132	131	0	−2.42%	1.82%	49.5
T15	30% SOC, 0.5 mm, H	135	120	0	−2.11%	2.04%	49.5
T9	30% SOC, 0.25 mm, H	261	62	168	−7.91%	13.57%	50.1
T19	100% SOC, 0.25 mm, H	229	68	157	−1.82%	2.78%	50.1
T21	30% SOC, 0.9 mm, C	122	116	0	−4.09%	2.85%	47.6
T31	100% SOC, 0.9 mm, C	150	69	81	−2.06%	2.51%	50.1
T27	30% SOC, 1.8 mm, C	268	2	266	n.d.	n.d.	50.2
T36	100% SOC, 1.8 mm, C	300	4	296	n.d.	n.d.	50.2

The notable deviation observed in cell T9 may be attributed to specific cell-level variations or possible manufacturing inconsistencies. Since the cells within each condition were subjected to identical mechanical loading, and since cell T9 was loaded under the mildest condition of the program, it is unlikely that mechanical stress alone caused the increased capacity loss. Variations in production, such as differences in electrode homogeneity or cell sealing quality, could be potential contributing factors. This hypothesis is supported by the fact that no similar deviation was observed in the other cells. It should be noted, however, that the cycling record of T9 is strongly fragmented (62 valid cycles out of 261 attempted), so the magnitude of the loss carries a higher uncertainty than that of the continuously recorded cells. Overall, the results suggest that the capacity changes over the recorded cycles are minor for most cells with a usable record; given the small number of cells per condition, the single reference cell and the non-uniform thermal boundary conditions discussed above, this should be regarded as an exploratory observation rather than a demonstration of suitability for repeated charge and discharge cycling under mechanical load.

3.5. Post-Mortem Analysis

For the post-mortem analysis, two specific cells, T5 and T36, were examined to analyze the effects of mechanical stress on the internal cell structure. The selection of these cells was based on different testing conditions: Cell T5 was tested at an SOC of 30% with an indentation depth of 0.5 mm using a spherical impactor, while Cell T36 was subjected to an SOC of 100% and an indentation depth of 1.8 mm using a cylindrical impactor. This selection enables the analysis of both moderate and extreme mechanical loads.

Before opening the cells, they were deeply discharged to eliminate potential hazards from remaining electrical energy and to ensure the safety of the subsequent analysis. The CT scan presented below (Figure 15) was performed beforehand, on the still-sealed cells; the structural findings this analysis relies on are therefore unaffected by the subsequent discharge and disassembly steps, which only precede the visual inspection of the opened electrode surfaces.

Cell opening was again performed under safe conditions in a glovebox to prevent contact with humidity and oxygen. This was necessary to preserve the original state of sensitive cell components, particularly the electrodes and separator. The glovebox was filled with a protective argon atmosphere to ensure an inert environment, where H_2O and O_2 concentrations were below 1 ppm.

After opening, the internal components were systematically removed and analyzed. Attention was given to the investigation of the electrode surfaces to identify potential mechanical damage such as cracks, abrasion, or delamination of the active material. The separators were also inspected for deformation or compression potentially caused by mechanical stress.

In Cell T5, a slight indentation was visible on the outer cell casing. However, no visible changes were observed in the active material beneath the casing. These results indicate that while the mechanical load affected the outer casing, the underlying cell layers remained unaffected. In contrast, Cell T36 showed a noticeable indentation at the cell head but no deformation along the casing. After opening, a minor indentation was visible at the top end of the active material near the cell's positive terminal. This deformation was confined to the uppermost layer of the cell, while deeper layers remained intact. A slight deformation of the overlying plastic cap was also observed, which was confirmed in detail by CT imaging. Figure 15 shows a CT scan of Cell T36, which was subjected to lateral indentation, particularly around the cell's positive terminal. The image is taken from the XY perspective.

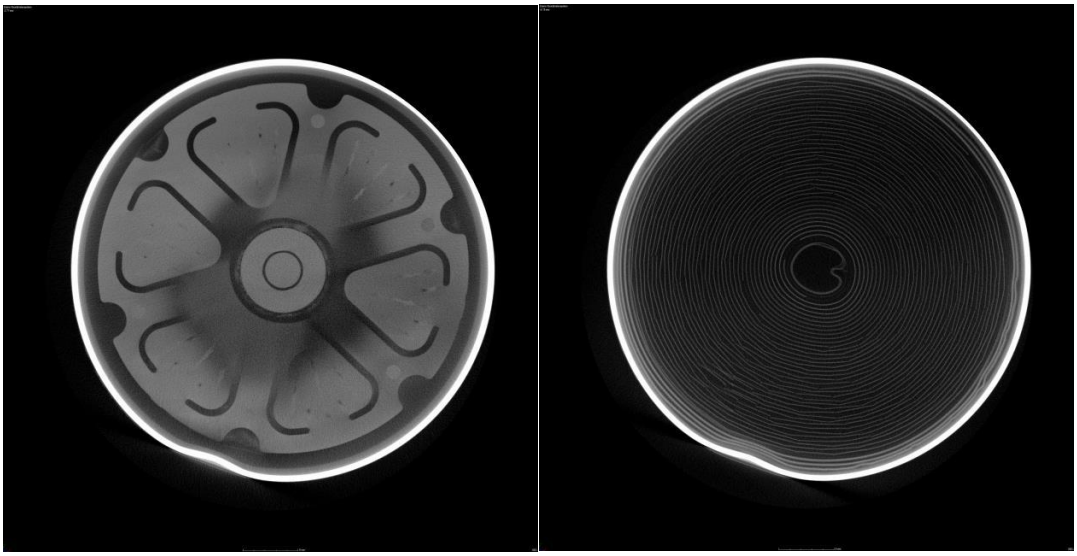


Figure 15. CT scan of cell T36 from the XY level (**left**: top section, **right**: bottom section).

A slight indentation of the cell wall and the outer layers of the active material can be seen pressing inward. This deformation results from the mechanical load applied in the area of the cell head. Despite the visible compression of the outer layers, this deformation did not lead to direct contact between the layers of the active material. The integral structure of the windings remains intact, and there are no visually or radiographically (CT) detectable signs of mechanical fractures or displacements that would be expected to cause an internal short circuit. This provides no immediate evidence of an internal short circuit and is consistent with prior cylindrical-cell crush and compression studies [18,21,24–26], which similarly identify a distinct deformation range that must be exceeded before short-circuit-inducing layer contact occurs. We note, however, that neither stable voltage and temperature during loading nor the absence of visible or CT-detectable damage rule out more subtle degradation such as localized separator damage or elevated internal resistance, which would require the electrical diagnostics discussed in Section 3.3. The minor indentation indicates a localized plastic deformation of the cell housing, while the central mechanical integrity of the cell remains unaffected. This is

corroborated quantitatively by the logged force-displacement curve for T36, which shows a residual displacement of ≈0.46 mm between loading and unloading, markedly larger than the ≤0.1 mm residual observed in the preliminary screening cell at the same nominal depth (Section 3.2). This indicates that T36 individually exceeded the local onset of plastic yielding, consistent with the cell-to-cell variability discussed elsewhere in this study (Section 3.4, cell T9), rather than indicating that 1.8 mm systematically causes plastic deformation across all cells.

The analysis shows that the cell can absorb a mechanical load in the cell head area to a certain extent without sustaining structural damage that could impair functionality. The fact that no internal short between the active material layers was observed suggests that the tested indentation depth remains below the threshold for critical mechanical damage. This finding aligns with the results of the cyclic aging tests, where no significant reduction in capacity was detected. The absence of visible or CT-detectable internal short-circuiting in the two post-mortem cells examined provides preliminary evidence of mechanical resilience under the specific quasi-static loading conditions tested, though this observation is based on a small sample and does not by itself establish suitability for safety-critical applications.

4. Summary and Key Findings

The non-destructive mechanical characterization of 4680-format cylindrical cells conducted in this study yields the following key findings:

- Range of predominantly reversible deformation: Loading and unloading curves returned to the initial contact position within measurement resolution up to indentation depths of 0.5 mm (hemispherical impactor) and 1.8 mm (cylindrical impactor) for the majority of tested cells. These depths are empirically determined thresholds for the specific cells and loading conditions examined and do not constitute a general elastic limit: localized plastic casing deformation with a residual displacement of 0.46 mm was observed in individual cells at these depths (Section 3.5).
- Peak force: The highest individual measurement across all tests was 9.16 kN (cell T36, 100% SOC, 1.8 mm, cylindrical impactor). The group-average maximum force for this condition was 7.92 kN (SD = 0.74 kN), without permanent damage in the majority of tested cells (Section 3.5). For the hemispherical impactor, mean peak forces ranged from 0.41 kN to 0.80 kN depending on condition and test campaign (Table A1).
- SOC dependence: Cells tested at 100% SOC consistently exhibited higher peak forces than those tested at 30% SOC, consistent with the prior literature on SOC-dependent stiffening of cylindrical cells [19,20,24,26].
- Thermal and electrical stability: No significant temperature rise and stable voltage were observed during loading, with no immediate evidence of an internal short circuit. More sensitive electrical diagnostics were not performed in this study.
- Cyclic aging: The unstressed reference cell showed a −2.69% capacity loss over 126 valid cycles, corresponding to 2.03% per 100 valid cycles. Mechanically loaded cells with a usable record fell between 1.82% and 2.85% per 100 valid cycles, with cell T9 the sole outlier at 13.57%. For the two cells cycled after 1.8 mm cylindrical indentation, too few valid cycles were recorded to permit any statement (exploratory, one to two cells per condition, single reference cell, and non-uniform thermal boundary conditions).
- Post-mortem/CT analysis: Deformation remained confined to the outermost jelly roll layer and the casing, with no contact between active-material layers and the winding structure remaining intact.

Taken together, these findings indicate that the tested commercial 4680-format cells (Supplier 1) tolerate the mechanical loads examined without loss of function, though generalization to 4680 cells from other manufacturers requires further validation (Section 2.1).

The conclusions of this study are based on a single quasi-static compressive load applied to isolated, unconfined cells. Several factors relevant to real Cell-to-X applications were not evaluated, including cyclic (repeated) mechanical loading, vibration, shock, confinement or potting within a pack structure; simultaneous mechanical contact between adjacent cells; and real-world vehicle loading spectra. The results presented here therefore provide preliminary evidence regarding the mechanical behavior of the tested cell type under the specific conditions examined and should not be interpreted as demonstrating the cells' definitive suitability as load-bearing structural vehicle components. This would require the additional loading scenarios outlined above and in Section 4.

The findings of this study provide a detailed foundation for the mechanical and electrical characterization of 4680 cylindrical cells and their potential integration into structural battery systems. However, there remains significant room for further investigation to deepen the understanding of these cells and their behavior in realistic operating environments. The following section outlines key avenues for future research, building on the insights gained in this work.

One important direction for future research lies in the further development of the Design of Experiments. The statistical planning carried out in this study provided valuable insights into the mechanical and electrical properties of the cells but holds potential for further optimization. Incorporating additional factors, such as varying temperature conditions during compression tests, could offer decisive contributions. Temperature has a substantial effect on the material properties of both the cell casing and the internal layers and thus influences the elastic and plastic behavior of the cells. Expanding the DoE to include temperature as a variable could enable systematic investigation of interactions between mechanical stress, thermal effects and electrochemical performance. Such studies could also reveal how the cells perform under extreme conditions, such as in cold or hot climates.

Another important focus for future work could be the extension of cyclic aging tests. In this study, a cycling program of 150 charge and discharge cycles was applied, of which between 2 and 131 cycles per cell met the validity criterion, providing only an initial impression of the cells' robustness under mechanical preloading. The cycling campaign was limited by over-temperature cut-offs of the cell tester and by non-uniform thermal boundary conditions between cycler channels; future work should use active temperature control and identical channel conditions for all cells, including the reference. Furthermore, the cycling results presented in this study are based on one or two cells per test condition and a single unstressed reference cell. Future work should include replicate cells per condition to enable a statistically robust separation of cell-to-cell variability from any genuine effect of prior mechanical loading on aging behavior. Furthermore, this study relied on voltage and surface temperature monitoring to assess electrical integrity during and after mechanical loading. These measures cannot rule out localized separator damage, a soft short circuit, or a gradual increase in internal resistance. Future work should include before-and-after measurements of DC resistance, electrochemical impedance spectroscopy (EIS), self-discharge, or relaxation voltage to more directly assess subtle or delayed electrical degradation. The authors are currently conducting a related study applying EIS measurements to mechanically deformed cells, which will address this question in more detail.

Long-term cycling could help identify and quantify gradual degradation mechanisms that become apparent only after several hundred or thousand cycles. These additional investigations would enable a more realistic assessment of the cells' service life in structural battery applications.

In addition to experimental approaches, research could be expanded using simulation-based methods. The finite element method (FEM) provides a powerful tool for in-depth analysis of the structural behavior of 4680 cells and their integration into battery systems such as Cell-to-X concepts. Simulative studies could enhance the understanding of mechanical stress

distributions within a cell block or module, especially under dynamic load conditions. Moreover, simulations could support the optimization of design parameters such as module stiffness, casing material properties, or the distribution of contact forces, contributing to improved mechanical design of structural battery systems.

Another aspect of future research could involve the integration of cells into modules or packs, with the replication of realistic load scenarios as found in automotive applications. In such setups, additional factors like vibrations, shock loads, or long-term pressure from neighboring cells and structural components could be investigated.

In summary, this study provides a solid foundation for the continued exploration of the mechanical and electrical characteristics of 4680 cylindrical cells. By expanding both experimental and simulation-based approaches, future studies can not only deepen the understanding of these cells but also contribute to the development of the next generation of structural battery systems that are more efficient, safer and more durable.

Author Contributions: Conceptualization, N.G. and R.J.; methodology, N.G. and R.J.; validation, N.G. and R.J.; formal analysis, N.G. and N.K.; resources, R.J.; data curation, R.J.; writing—original draft preparation, N.G.; writing—review and editing, N.G.; visualization, R.J.; supervision, N.K., H.H. and A.K.; project administration, N.K.; funding acquisition, A.K. and H.H. All authors have read and agreed to the published version of the manuscript.

Funding: This research was funded by the German federal ministry for economic affairs and energy, grant number 16BZF359G.

Data Availability Statement: The data presented in this study are available on request from the corresponding author due to privacy reasons.

Acknowledgments: During the preparation of this study, the authors used Claude Opus 5 for processing the raw cycler data and for grammar correction. The authors reviewed and edited the output and take full responsibility for the content of this publication.

Conflicts of Interest: Author Rizwan Javed is employed by RheinNetz GmbH. The remaining authors declare that the research was conducted in the absence of any commercial or financial relationships that could be construed as a potential conflict of interest.

Abbreviations

The following abbreviations are used in this manuscript:

BTC	Battery Testing Chamber
CT	Computed Tomography
CTC	Cell-to-Chassis
CTP	Cell-to-Pack
CTX	Cell-to-X
DOE	Design of Experiments
EV(s)	Electric Vehicle(s)
FEM	Finite Element Method
ICE	Internal Combustion Engine
ISO	International Organization for Standardization
MTC	Module-to-Chassis
NMC811	Nickel Manganese Cobalt oxide (Ni:Mn:Co = 8:1:1)
OCV	Open Circuit Voltage
SEI	Solid Electrolyte Interphase
SOC	State of Charge

Appendix A

Table A1. Measurement results by group. Campaign 1 and campaign 2 denote the two test campaigns between which the reference position of the actuator was changed; hemispherical groups are therefore not pooled across campaigns. Group 5 contains a single specimen.

Group	Impactor	Depth [mm]	SOC [%]	Campaign	n	Mean Force [N]	SD [N]	CV [%]	95% CI [N]
1	H	0.5	30	1	5	796.3	±66.5	8.35	713.7–878.8
2	H	0.5	30	2	4	501.6	±81.2	16.19	372.4–630.7
3	H	0.25	100	1	3	643.0	±14.7	2.28	606.4–679.5
4	H	0.25	100	2	4	405.4	±13.5	3.33	383.9–426.8
5	H	0.25	30	2	1	360.0	n.a.	n.a.	n.a.
6	C	0.9	30	2	5	2441.2	±94.7	3.88	2323.6–2558.8
7	C	1.8	30	2	5	5111.8	±538.3	10.53	4443.4–5780.2
8	C	0.9	100	2	5	2601.2	±184.3	7.08	2372.4–2830.0
9	C	1.8	100	2	5	7917.2	±741.9	9.37	6996.1–8838.3

Table A2. Individual peak forces of all tests.

Group	Cell IDs	Individual Peak Forces [N]
1	T1, T2, T3, T4, T5	706.7; 853.1; 866.2; 756.9; 798.5
2	T11, T12, T13, T15	442.5; 606.0; 432.3; 525.5
3	T6, T7, T8	626.0; 652.2; 650.7
4	T16, T17, T18, T19	404.5; 395.1; 397.2; 424.7
5	T9	360.0
6	T21, T22, T23, T24, T25	2471; 2465; 2498; 2274; 2498
7	T26, T27, T28, T29, T30	5911; 5186; 5077; 4977; 4408
8	T31, T32, T33, T34, T35	2825; 2357; 2483; 2706; 2635
9	T36, T37, T38, T39, T40	9159; 7791; 7176; 7620; 7840

References

1. König, A.; Nicoletti, L.; Schröder, D.; Wolff, S.; Waclaw, A.; Lienkamp, M. An Overview of Parameter and Cost for Battery Electric Vehicles. *World Electr. Veh. J.* **2021**, *12*, 21. https://doi.org/10.3390/wevj12010021.
2. IEA, International Energy Agency. *Global EV Outlook 2024: Moving Towards Increased Affordability 2024*; International Energy Agency: Paris, France, 2024.
3. Kim, T.; Song, W.; Son, D.-Y.; Ono, L.K.; Qi, Y. Lithium-ion batteries: Outlook on present, future, and hybridized technologies. *J. Mater. Chem. A* **2019**, *7*, 2942–2964. https://doi.org/10.1039/c8ta10513h.
4. BMW Group. The Fice Steps to the Battery Cell in the CMCC Pilot Series. Available online: https://www.bmwgroup.com/en/report/2023/bmw-group-report/cell-intelligence/index.html (accessed on 4 August 2026).
5. Musk, E.; Baglino, D.B. Tesla Battery Day Presentation, 22 September 2020.
6. Li, S.; Marzook, M.W.; Zhang, C.; Offer, G.J.; Marinescu, M. How to enable large format 4680 cylindrical lithium-ion batteries. *Appl. Energy* **2023**, *349*, 121548. https://doi.org/10.1016/j.apenergy.2023.121548.
7. Yourey, W. Cell Design Considerations and Impact on Energy Density—A Practical Approach to EV Cell Design. *World Electr. Veh. J.* **2023**, *14*, 279. https://doi.org/10.3390/wevj14100279.
8. Pegel, H.; Wycisk, D.; Sauer, D.U. Influence of cell dimensions and housing material on the energy density and fast-charging performance of tabless cylindrical lithium-ion cells. *Energy Storage Mater.* **2023**, *60*, 102796. https://doi.org/10.1016/j.ensm.2023.102796.
9. Kampker, A.; Heimes, H.H.; Offermanns, C.; Vienenkötter, J.; Robben, T. Framework and Classification of Battery System Architectures. *World Electr. Veh. J.* **2023**, *14*, 88. https://doi.org/10.3390/wevj14040088.
10. Pampel, F.; Pischinger, S.; Teuber, M. A systematic comparison of the packing density of battery cell-to-pack concepts at different degrees of implementation. *Results Eng.* **2022**, *13*, 100310. https://doi.org/10.1016/j.rineng.2021.100310.

11. Liu, Y.; Yang, Z.; Huang, X.; Tan, J. A review of cell-to-body (CTB) battery-structure integration design for electric vehicles. *Front. Mech. Eng.* **2026**, *12*, 1825484. https://doi.org/10.3389/fmech.2026.1825484.
12. Jin, B.; Liao, L.; Shen, X.; Mei, Z.; Du, Q.; Liang, L.; Lei, B.; Du, J. Advancement in Research on Silicon/Carbon Composite Anode Materials for Lithium-Ion Batteries. *Metals* **2025**, *15*, 386. https://doi.org/10.3390/met15040386.
13. Xiong, Y.; Pan, Y.; Wu, L.; Liu, B. Effective weight-reduction- and crashworthiness-analysis of a vehicle's battery-pack system via orthogonal experimental design and response surface methodology. *Eng. Fail. Anal.* **2021**, *128*, 105635. https://doi.org/10.1016/j.engfailanal.2021.105635.
14. Agarwal, A.; Cavicchioli Batista, R.; Tashi. Crashworthiness Evaluation of Electric Vehicle Battery Packs Using Honeycomb Structures and Explicit Dynamic Analysis. *E3S Web Conf.* **2024**, *519*, 04010. https://doi.org/10.1051/e3sconf/202451904010.
15. Belingardi, G.; Scattina, A. Battery Pack and Underbody: Integration in the Structure Design for Battery Electric Vehicles—Challenges and Solutions. *Vehicles* **2023**, *5*, 498–514. https://doi.org/10.3390/vehicles5020028.
16. Greve, L.; Fehrenbach, C. Mechanical testing and macro-mechanical finite element simulation of the deformation, fracture, and short circuit initiation of cylindrical Lithium ion battery cells. *J. Power Sources* **2012**, *214*, 377–385. https://doi.org/10.1016/j.jpowsour.2012.04.055.
17. Sahraei, E.; Campbell, J.; Wierzbicki, T. Modeling and short circuit detection of 18650 Li-ion cells under mechanical abuse conditions. *J. Power Sources* **2012**, *220*, 360–372. https://doi.org/10.1016/j.jpowsour.2012.07.057.
18. Xu, J.; Liu, B.; Wang, L.; Shang, S. Dynamic mechanical integrity of cylindrical lithium-ion battery cell upon crushing. *Eng. Fail. Anal.* **2015**, *53*, 97–110. https://doi.org/10.1016/j.engfailanal.2015.03.025.
19. Xu, J.; Liu, B.; Hu, D. State of Charge Dependent Mechanical Integrity Behavior of 18650 Lithium-ion Batteries. *Sci. Rep.* **2016**, *6*, 21829. https://doi.org/10.1038/srep21829.
20. Xu, J.; Liu, B.; Wang, X.; Hu, D. Computational model of 18650 lithium-ion battery with coupled strain rate and SOC dependencies. *Appl. Energy* **2016**, *172*, 180–189. https://doi.org/10.1016/j.apenergy.2016.03.108.
21. Zhu, J.; Zhang, X.; Sahraei, E.; Wierzbicki, T. Deformation and failure mechanisms of 18650 battery cells under axial compression. *J. Power Sources* **2016**, *336*, 332–340. https://doi.org/10.1016/j.jpowsour.2016.10.064.
22. Wang, W.; Yang, S.; Lin, C.; Shen, W.; Lu, G.; Li, Y.; Zhang, J. Investigation of mechanical property of cylindrical lithium-ion batteries under dynamic loadings. *J. Power Sources* **2020**, *451*, 227749. https://doi.org/10.1016/j.jpowsour.2020.227749.
23. Huang, J.; Shen, W.; Lu, G. Mechanism of failure behaviour and analysis of 18650 lithium-ion battery under dynamic loadings. *Eng. Fail. Anal.* **2023**, *153*, 107588. https://doi.org/10.1016/j.engfailanal.2023.107588.
24. Zhang, X.; Zhang, T.; Liu, N.; Yin, X.; Wu, X.; Han, H.; Wang, Q.; Zhang, Y. Dynamic crushing behaviors and failure of cylindrical lithium-ion batteries subjected to impact loading. *Eng. Fail. Anal.* **2023**, *154*, 107653. https://doi.org/10.1016/j.engfailanal.2023.107653.
25. An, Z.; Shi, T.; Du, X.; An, X.; Zhang, D.; Bai, J. Experimental study on the internal short circuit and failure mechanism of lithium-ion batteries under mechanical abuse conditions. *J. Energy Storage* **2024**, *89*, 111819. https://doi.org/10.1016/j.est.2024.111819.
26. Huang, Z.; Zhang, X.; Liu, N.; Gu, L.; An, L.; Zhou, W. Failure mechanisms and acoustic responses of cylindrical lithium-ion batteries under compression loadings. *Eng. Fail. Anal.* **2024**, *163*, 108594. https://doi.org/10.1016/j.engfailanal.2024.108594.
27. *ISO 12405-4:2018*; Electrically Propelled Road Vehicles—Test Specification for Lithium-Ion Traction Battery Packs and Systems. ISO: Geneva, Switzerland, 2018. Available online: https://www.iso.org/standard/71407.html (accessed on 4 August 2026).
28. Gorsch, J.; Schneiders, J.; Frieges, M.; Kisseler, N.; Klohs, D.; Heimes, H.; Kampker, A.; Muñoz Castro, M.; Sie-becke, E. Contrasting a BYD Blade prismatic cell and Tesla 4680 cylindrical cell with a teardown analysis of design and performance. *Cell Rep. Phys. Sci.* **2025**, *6*, 102453. https://doi.org/10.1016/j.xcrp.2025.102453.
29. Wu, X.; Mou, X.; Bu, L.; Han, X. Battery and Battery Module and Battery Pack Having the Same. CN217134494U, 5 August 2022.
30. Ghandily, N.; Nakrani, P.; Kisseler, N.; Heimes, H.; Kampker, A. Overview of the current state of research on thermal runaway and thermal propagation testing of lithium-ion batteries. *Cell Rep. Phys. Sci.* **2026**, *7*, 103111. https://doi.org/10.1016/j.xcrp.2026.103111.
31. Liu, Y.; Ju, L.; Jia, Z.Z.; Cheng, Z.; Min, Y.; Mei, W.; Qin, P.; Wang, Q. Experimental study on the internal pressure evolution of large-format $LiFePO_4$ battery during thermal runaway. *J. Energy Storage* **2024**, *102*, 114196. https://doi.org/10.1016/j.est.2024.114196.

32. UN ECE. *Uniform Provisions Concerning the Approval of Vehicles with Regard to Specific Requirements for the Electric Power Train*, 2nd ed.; UNECE: Geneva Switzerland, 2021. Available online: https://unece.org/sites/default/files/2024-01/R0100r3e.pdf (accessed on 4 August 2026).
33. *SAE J 2380-2009*; Vibration Testing of Electric Vehicle Batteries. SAE International: Warrendale, PA, USA, 2009. Available online: https://webstore.ansi.org/standards/sae/sae23802009j2380 (accessed on 4 August 2026).

Disclaimer/Publisher's Note: The statements, opinions and data contained in all publications are solely those of the individual author(s) and contributor(s) and not of MDPI and/or the editor(s). MDPI and/or the editor(s) disclaim responsibility for any injury to people or property resulting from any ideas, methods, instructions or products referred to in the content.